Thermal effects connected to crystallization dynamics: A lattice Boltzmann study

Q. Tan [a], S.A. Hosseini [a,c,*], A. Seidel-Morgenstern [b], D. Thévenin [a], H. Lorenz [b]

[a] *Laboratory of Fluid Dynamics and Technical Flows, University of Magdeburg "Otto von Guericke", Magdeburg, 39106, Germany*
[b] *Max Planck Institute for Dynamics of Complex Technical Systems (MPI DCTS), Magdeburg, 39106, Germany*
[c] *Department of Mechanical and Process Engineering, ETH Zürich, 8092, Switzerland*

ARTICLE INFO

ABSTRACT

The possible impact of temperature differences during crystal growth is investigated in this study. The organic molecule considered is mandelic acid, an important component for the pharmaceutical industry. The productivity of generating pure mandelic acid crystals are largely determined by the growth process. Reaction conditions, purity of the components, supersaturation, temperature, but possibly also temperature gradients play a central role during crystal growth. In this study a numerical model based on a hybrid solver combining the lattice Boltzmann method with finite differences is developed to model the crystallization dynamics of (S)-mandelic acid (S-ma) taking quantitatively into account temperature effects. At first, the fourth-order finite-difference method used to model energy and species conservation is validated. Then, comparisons are carried out regarding temperature changes within the single-crystal growth cell. In practice, the molar heat generation at the crystal interface shows only a small effect on the temperature field in the surrounding domain, with temperature differences below 1.5 degree. Finally, the study is extended to investigate the impact of forced convection on the crystal habits while taking into account temperature differences.

1. Introduction

Mandelic acid and its derivatives are frequently used compounds in the pharmaceutical industry. It exists as two pure enantiomers and in the racemic form, with strong consequences on its pharmacological properties (Chlebus, 2006). It is also used for the further organic synthesis of pharmaceuticals, such as esters of mandelic acid generating homatropine for eye drops. Mandelic acid is well known for its anti-aging effects on the skin along with antibacterial functions in treating acne (Emelýanenko et al., 2018). Furthermore, the manufacture of many rubbers, adhesives, and plastic materials requires mandelic acid as an intermediate substance. (S)- and (R)-mandelic acid are the two enantiomeric forms. Enantiopure substances are required for most pharmaceutical applications (Brittain, 2002). Crystallization is widely used for the separation of enantiomers relying on classical resolution, or preferential crystallization approaches (Lorenz and Seidel-Morgenstern, 2014). During crystallization, essential properties of the crystalline products (e.g., purity, shape, sizes (Briesen, 2006)) are determined by the growth process, which again depends on the conditions within the crystallizer. The reaction conditions, such as supersaturation, temperature, other components possibly present in the solution (impurities, additives) play a central role for crystal growth. Many experimental studies have been conducted concerning crystallization-based enantio-separation processes. Of particular interest for the present work are measurements regarding growth kinetics of mandelic acid, e.g. Alvarez Rodrigo et al. (2004), Lorenz and Seidel-Morgenstern (2014), Coquerel (2006), Gänsch et al. (2021), Gou et al. (2012), Perlberg et al. (2005), Srisanga et al. (2015) and Codan et al. (2013). Most of the studies carried out up to now relied on the assumption of a perfectly homogeneous temperature during crystallization. Typically, experimental temperature measurements rely on a single sensor (point measurement), so that possible temperature gradients could not be tracked. Since only small temperature differences are expected, experimental investigations regarding temperature effects during crystal growth would be challenging and costly.

Numerical simulations using accurate and efficient algorithms can in this case complement or replace such experiments and provide corresponding answers. In recent years, much effort has been put on developing mathematical models and numerical algorithms suitable for describing crystal habit and size of crystals (Karma and Rappel, 1998; Younsi and Cartalade, 2016), also for enantiopure (S)-mandelic acid (Tan et al., 2022, 2023). The phase-field method has become one of the most popular approaches to simulate crystal growth. It
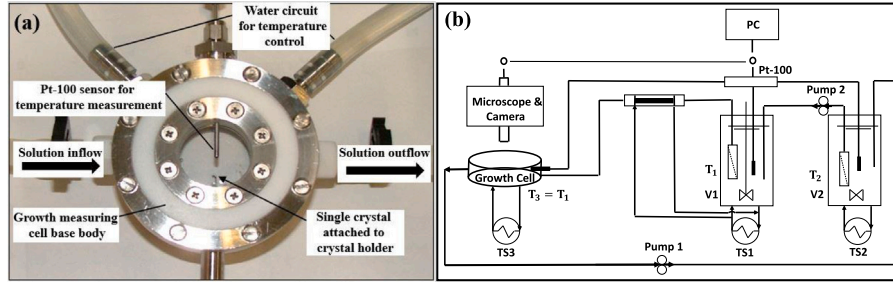
Fig. 1. Single-crystal growth cell used for all experiments: (a) photograph; (b) Schematic diagram of experimental arrangement for the measurement of a single crystal growth rates (Gou et al., 2012; Bianco, 2009).

is a powerful tool for modeling structural evolution of materials and crystals (Vakili et al., 2020; Subhedar et al., 2020; Schiedung et al., 2020). It is now widely used to investigate solidification (Boettinger et al., 2002; Nestler and Wheeler, 2002) and grain growth (Chen and Yang, 1994; Takaki et al., 2016; Karma and Rappel, 1998; Tourret et al., 2017). The phase-field approach has also been used in combination with the lattice Boltzmann method, now widely recognized as an efficient alternative to classical tools, to simulate solidification processes (Younsi and Cartalade, 2016; Lin et al., 2014; Wang et al., 2019; Rojas et al., 2015; Zirdehi and Varnik, 2019). This approach can reproduce numerically the solid–liquid interface interactions and the hydrodynamic effects affecting the habits of growing crystals (Henniges et al., 2017; Medvedev et al., 2006; Sakane et al., 2018; Chakraborty and Chatterjee, 2007; Tan et al., 2022, 2023). While widely used in the literature for hydrodynamic simulations the lattice Boltzmann method is known to suffer from Gibbs-type oscillations near sharp interfaces and instability issues in the limit of vanishing diffusion coefficients. Furthermore, the classical passive-scalar lattice Boltzmann solvers cannot take into account flows with variable density and/or specific heat capacity. For such flows the models need to be extended, see for instance (Hosseini et al., 2019b). In such cases an interesting alternative is to replace the solvers for the scalar fields, e.g. species and temperature, with classical finite-difference solvers with discontinuity-capturing schemes for the advection term. The corresponding finite-difference solvers are then coupled to a lattice Boltzmann approach for describing hydrodynamics. Such hybrid approaches have been increasingly used in the past years for applications such as combustion, see for instance (Hosseini et al., 2019c, 2020, 2022).

In the present work the crystal growth of (S)-mandelic acid is studied in detail using a hybrid lattice Boltzmann/finite-difference method under different reaction conditions and taking into account temperature difference changes; additionally, possible convection (sometimes also called ventilation) effects will be considered. At the difference of previous works, the enthalpy production due to mandelic acid lattice integration is included in the model and an energy balance equation is solved in the whole domain; in this manner, the effects of possible temperature gradients within the crystallizer are fully taken into account. In companion experiments, well-characterized seed crystals must be produced from supersaturated aqueous (S)-mandelic acid solutions. The single grain growth is then tracked, the growing crystal being inserted into a dedicated measurement cell. For the present studies focusing on thermal effects: (1) the growth rate of the crystal was investigated for different crystallization temperatures in the growth cell; (2) numerically, heat generation is taken into account at the crystal interface and temperature changes are solved for within the entire growth cell. Finally, (3) the impact of convection effects on crystal habit is studied at different Reynolds numbers. Baffles are additionally placed in the cell to support symmetrical crystal growth.

2. Numerical methods

2.1. Governing equations

2.1.1. Diffuse-interface formulation: governing equations

In the phase-field method solid growth dynamics are expressed via a non-dimensional order parameter, ϕ, going from $(+1)$ in the solid to (-1) in the pure liquid phase. The space/time evolution equations are written as (Jeong et al., 2001; Beckermann et al., 1999):

$$\tau_0 a_s^2(\mathbf{n}) \frac{\partial \phi}{\partial t} = W_0^2 \boldsymbol{\nabla} \cdot \left(a_s^2(\mathbf{n})\right) \boldsymbol{\nabla} \phi + W_0^2 \boldsymbol{\nabla} \cdot \left(|\boldsymbol{\nabla}\phi|^2 \frac{\partial[a(\mathbf{n})^2]}{\partial \boldsymbol{\nabla}\phi}\right)$$
$$+ (\phi - \phi^3) + (\lambda_1 U + \lambda_2 \theta)(1 - \phi^2)^2, \tag{1}$$

and regarding normalized supersaturation U:

$$\frac{\partial U}{\partial t} + \left(\frac{1-\phi}{2}\right) \boldsymbol{u} \cdot \boldsymbol{\nabla} U = D \boldsymbol{\nabla} \cdot (q(\phi)\boldsymbol{\nabla} U) - \frac{1}{2}\frac{\partial \phi}{\partial t}, \tag{2}$$

and temperature θ:

$$\frac{\partial T}{\partial t} + \left(\frac{1-\phi}{2}\right) \boldsymbol{u} \cdot \boldsymbol{\nabla} T = \frac{1}{\rho \widetilde{c_p}} \boldsymbol{\nabla} \rho \widetilde{c_p} \widetilde{\kappa} \cdot \boldsymbol{\nabla} T + \frac{1}{2}\frac{\Delta H_{\text{cryst}}}{\widetilde{c_p}}\frac{\partial \phi}{\partial t}, \tag{3}$$

where $\tau = \tau_0 a_s^2(\mathbf{n})$. The coefficient λ_1 and λ_2 describes the strength of the coupling between the phase-field and the supersaturation field U, the temperature field T, respectively. $\theta = (T - T_1)/T_1$ is the normalized temperature in the phase field equation. T_1 is the constant temperature in the growth cell(see Fig. 1). Both U and θ contribute to the driving force for the crystal growth. The parameter $\lambda_1 = \frac{\tau_0}{W_0^2} \cdot \frac{D}{a_2}$, where D is the diffusion coefficient of the solution and $a_2 = 0.6267$ (Ramirez et al., 2004). Here $\lambda_1 = 3.0$ (Tan et al., 2023). The parameter τ_0 denotes the characteristic time and W_0 the characteristic width of the diffuse interfaces. In Eq. (1), the quantity $\mathbf{n} = -\frac{\boldsymbol{\nabla}\phi}{|\boldsymbol{\nabla}\phi|}$ is the unit vector normal to the crystal interface pointing from solid to fluid, while $a_s(\mathbf{n})$ is the surface tension anisotropy function. In the context of the hexagonal mandelic acid crystal growth, this quantity is defined as (Karma and Rappel, 1998):

$$a_s(\mathbf{n}) = 1 + \varepsilon_s \cos(6\varphi), \tag{4}$$

with $\varphi = \arctan(n_y/n_x)$ considering the two spatial dimensions x and y. The numerical parameter ε_s characterizes the anisotropy strength, and is set in the present study to $\varepsilon_s = 0.05$ following (Karma and Rappel, 1996). The term $(\phi - \phi^3)$ is the derivative of the double-well potential. The last term in Eq. (1) is a source term accounting for the coupling between supersaturation U, temperature θ, and order parameter ϕ. There, $(1 - \phi^2)^2$ is an interpolation function minimizing the bulk potential at $\phi = \pm 1$.

In Eq. (2), $\boldsymbol{u}$ denotes the local fluid velocity while $q(\phi) = (1 - \phi)$ is a function canceling out diffusion within the solid. As a consequence, solute transport is assumed to take place only within the fluid phase

Table 1
Physical parameters used for modeling single S-ma crystal growth at temperature of 25 °C.

Property	Value	Unit	Ref.
Enthalpy of crystallization ΔH_{cryst}	−18.5	kJ/mol	Emelýanenko et al. (2018)
Specific heat capacity for solid $c_{p,S}$	160.5	J/mol K	Sapoundjiev et al. (2005)
Specific heat capacity for liquid $c_{p,L}$	75	J/mol K	Sapoundjiev et al. (2005)
Thermal diffusivity for solid κ_S	1.1	mm^2/s	Slack (1979)
Thermal diffusivity for liquid κ_L	0.146	mm^2/s	Speedy (1982)
Crystal growth rate constant k_0	1.0×10^{-5}	cm/s	Zhang et al. (2010)
Density of solid ρ_S	1.341	g/cm^3	https://www.chemicalbook.com/ChemicalProductProperty_EN_CB7428618.htm
Density of fluid ρ_L	1.0	g/cm^3	Patterson and Morris (1994)

(one-sided model). The parameter D is the diffusion coefficient of (S)-mandelic acid in water. Normalized supersaturation U is later defined in Eq. (23); its transport equation is given by Eq. (2).

In Eq. (3), $\tilde{\kappa}$ is the thermal diffusivity in the single-crystal growth cell, which is defined as:

$$\tilde{\kappa} = \frac{(1-\phi)\kappa_L + (1+\phi)\kappa_S}{2}, \tag{5}$$

where κ_L is the thermal diffusivity for the solution and κ_s is for the solid. The quantity $\tilde{\kappa}$ tracks the different values of thermal diffusivity between the liquid and solid phases. Similarly, for specific heat capacity:

$$\tilde{c}_p = \frac{(1-\phi)c_{p,L} + (1+\phi)c_{p,S}}{2}. \tag{6}$$

where $c_{p,L}$ is the specific capacity for the liquid and $c_{p,S}$ is for the crystal. The quantity ΔH_{cryst} represents the energy difference per mole of S-ma between the crystal solid and aqueous phases (see Table 1).

2.1.2. Flow field formulation

The mass conservation (or continuity) equation reads for this incompressible system:

$$\nabla \cdot \left[\frac{1-\phi}{2} \boldsymbol{u} \right] = 0, \tag{7}$$

where $\boldsymbol{u}$ is the velocity of the flow field. The momentum conservation equation is as follows:

$$\frac{\partial}{\partial t} \left[\frac{1-\phi}{2} \boldsymbol{u} \right] + \boldsymbol{u} \cdot \nabla \left[\frac{1-\phi}{2} \boldsymbol{u} \right] + \left(\frac{1-\phi}{2} \right) \frac{\nabla P}{\rho_0}$$
$$= \nu \nabla^2 \left[\frac{1-\phi}{2} \boldsymbol{u} \right] - \nu \frac{h(1+\phi)^2(1-\phi)}{4W_0^2} \boldsymbol{u}, \tag{8}$$

where t is time, P pressure, ρ_0 the liquid phase density, ν kinematic viscosity, W_0 interface thickness and h a constant (equal to 2.757) that ensures that the interface shear is correct for a simple shear flow (Beckermann et al., 1999).

2.2. Numerical methods

2.2.1. Flow field solver with LBM

The flow field behavior (described by the incompressible Navier–Stokes and continuity equations) is modeled using the classical LB formulation consisting of the now-famous stream-collide operators:

$$f_\alpha \left(\boldsymbol{x} + \boldsymbol{c}_\alpha \delta t, t + \delta t \right) - f_\alpha (\boldsymbol{x}, t) = \delta t \Omega_\alpha (\boldsymbol{x}, t) + \delta t \boldsymbol{F}, \tag{9}$$

where $\boldsymbol{F}$ is the external force. Here, $\boldsymbol{F}$ is used to represent the interaction with the solid phase following (Beckermann et al., 1999):

$$F = -\frac{h\nu(1+\phi)^2(1-\phi)\boldsymbol{u}}{4W_0^2} \tag{10}$$

where h is a dimensionless constant, chosen as $h = 2.757$ (Beckermann et al., 1999). Due to the absence of fluid velocity within the solid crystal, the velocity variable $\boldsymbol{u}$ is updated as:

$$\boldsymbol{u}^* = \frac{(1-\phi)}{2} \boldsymbol{u}, \tag{11}$$

and the corrected fluid velocity $\boldsymbol{u}^*$ is used in the equilibrium distribution function (Beckermann et al., 1999). The collision operator Ω_α follows the linear Bhatnagar–Gross–Krook (BGK) approximation:

$$\Omega_\alpha = \frac{1}{\tau} \left[f_\alpha^{(eq)} - f_\alpha \right], \tag{12}$$

where $f_\alpha^{(eq)}$ is the discrete isothermal equilibrium distribution function (EDF) defined as:

$$f_\alpha^{(eq)} = \rho w_\alpha \sum_i \frac{1}{i! c_s^{2i}} a_i^{(eq)}(\boldsymbol{u}) : \mathcal{H}_i(\boldsymbol{c}_\alpha), \tag{13}$$

where $a_i^{(eq)}$ and $\mathcal{H}_i(\boldsymbol{c}_\alpha)$ are the corresponding multivariate Hermite coefficients and polynomials of order i, with c_s the lattice sound speed corresponding to the speed of sound at the stencil reference temperature, and w_α the weights associated to the Gauss–Hermite quadrature (Shan et al., 2006). Further information on the expansion along with detailed expressions of the EDF can be found in Shan et al. (2006), Hosseini et al. (2019a) and Hosseini (2020). In the present work, an extended range of stability is obtained by using a central Hermite multiple relaxation time (MRT) implementation; corresponding details can be found in Hosseini et al. (2021). The relaxation time η_τ is tied to the fluid kinematic viscosity as:

$$\eta_\tau = \frac{\nu}{c_s^2} + \frac{\delta t}{2}. \tag{14}$$

Conserved variables, i.e., density and momentum are defined as moments of the discrete distribution function:

$$\rho = \sum_\alpha f_\alpha, \tag{15}$$

$$\rho \boldsymbol{u} = \sum_\alpha \boldsymbol{c}_\alpha f_\alpha. \tag{16}$$

2.2.2. LBM for phase-field equation

The phase-field equation is modeled using a modified lattice Boltzmann (LB) scheme implemented as (Walsh and Saar, 2010; Cartalade et al., 2016):

$$a_s^2(\boldsymbol{n}) h_\alpha(\boldsymbol{x} + \boldsymbol{c}_\alpha \delta x, t + \delta t) = h_\alpha(\boldsymbol{x}, t)$$
$$- \left(1 - a_s^2(\boldsymbol{n}) \right) h_\alpha(\boldsymbol{x} + \boldsymbol{c}_\alpha \delta x, t) -$$
$$\frac{1}{\eta_\phi(\boldsymbol{x}, t)} \left[h_\alpha(\boldsymbol{x}, t) - h_\alpha^{eq}(\boldsymbol{x}, t) \right] + w_\alpha Q_\phi(\boldsymbol{x}, t) \frac{\delta t}{\tau_0}, \tag{17}$$

where the scalar function Q_ϕ is the source term of the phase-field defined as:

$$Q_\alpha = (\phi - \phi^3) + \lambda(U + \theta)(1 - \phi^2)^2, \tag{18}$$

while the EDF h_α^{eq} is defined as:

$$h_\alpha^{eq} = w_\alpha \left(\phi - \frac{1}{c_s^2} \boldsymbol{c}_\alpha \cdot \frac{W_0^2}{\tau_0} |\nabla \phi|^2 \frac{\partial(a_s(\boldsymbol{n})^2)}{\partial \nabla \phi} \frac{\delta t}{\delta x} \right). \tag{19}$$

where $\nabla \phi$ is calculated by directional derivatives with higher-order isotropy (Tan et al., 2022):

$$\nabla \phi = \frac{1}{c_s^2} \sum_{\alpha=0}^{Q} w_\alpha \left(|c_\alpha|^2 \right) \phi \left(x + c_\alpha \right) c_\alpha \tag{20}$$
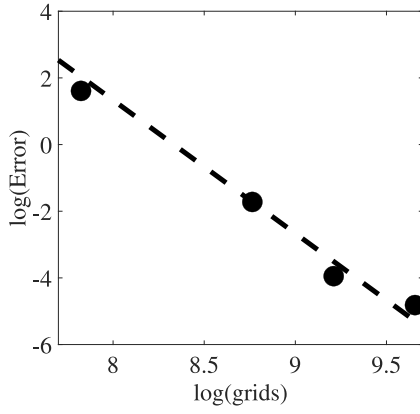
Fig. 2. Scaling of the l^2 error norm as obtained from the grid convergence study. Black markers represent error data from the simulations (see Table 2) while the black dashed line displays the theoretical -4 slope.

Fig. 3. Schematic of adiabatic cell box in 3D.

where $w_\alpha \left(|c_\alpha|^2 \right)$ are the weights associated to each layer of neighboring nodes maximizing isotropy (Shan, 2006). The local value of the order parameter ϕ is computed as:

$$\phi = \sum_\alpha h_\alpha, \tag{21}$$

while the relaxation is set to:

$$\eta_\phi = \frac{1}{c_s^2} a_s^2(\boldsymbol{n}) \frac{W_0^2}{\tau_0} + \frac{\delta t}{2}. \tag{22}$$

2.2.3. Finite-difference solver for species and energy equations

Balance equations for supersaturation and temperature are solved using a finite-difference scheme with a simple first-order time-stepping coupled to a fourth-order central discretization in space for diffusion terms and a third-order weighted essentially non-oscillatory (WENO) approximation for convective terms (Liu et al., 1994). Related researches are investigated from Liu et al. (1994), Cockburn et al. (1998) and Shu (2020).

2.3. Evaluation of thermo-physical properties

The physical parameters of the pure (S)-mandelic acid at temperature $T = 298.15$ K (or 25 °C) are listed in Table 1. The enthalpy of crystallization ΔH_{cryst} characterizes the energy difference per mole of S-ma between the solid and liquid(melt) phase and is represented here as negative value of the enthalpy of fusion (Emelýanenko et al., 2018). The value of specific heat capacity $c_{p,L}$ is that of water (being by far the dominating component) and $c_{p,S}$ is for racemic MA (Sapoundjiev et al., 2005). Furthermore, κ_S denotes the thermal diffusivity of the crystal and κ_L represents the thermal diffusivity of water (Slack, 1979; Speedy, 1982), while D is the diffusion coefficient for the solution (Tanner, 1983).

3. Experimental setup

All experimental data for the single S-ma crystal growth rate in the growth cell have been obtained from Gou et al. (2012), Bianco (2009). The corresponding experimental setup is illustrated in Fig. 1. A supersaturated aqueous solution of mandelic acid is pumped into a constant-temperature cylindrical crystallization cell, with solution temperatures varying between 20 and 30 °C. The temperature within the cell is maintained constant via a water-based cooling/heating system connected to a Pt-100 sensor monitoring the temperature at the center of the cell. Vessel 2, denoted V2 in Fig. 1b contains a saturated
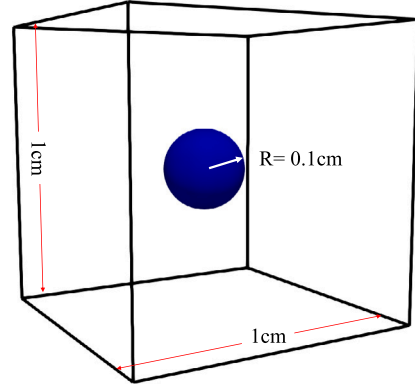
solution at temperature T_2 while vessel 1 (V1) was set to a lower temperature T_1, corresponding to the temperature of the cell. To create the supersaturated solution, the initially saturated solution in V2 is pumped into V1 and cooled down to T_1 before entering the growth cell. This effectively allows to control the supersaturation level of the incoming solution by choosing temperature T_1. Based on the solutions in the two vessels, the normalized supersaturation is defined as (Mullin, 2001):

$$U = \frac{C_{sat,2} - C_{sat,1}}{C_{sat,1}} \tag{23}$$

To start the experiment, the supersaturated solution is continuously pumped from vessel 1 to the growth cell, in which a single (S)-mandelic crystal is glued on the pin head of a crystal holder. Then, the solution is recycled to vessel 2 and the concentration of the solution is compensated. In that way, a stable degree of supersaturation is guaranteed during the whole process. A microscope with camera (Stemi2000C, Carl Zeiss Co.) is used to take pictures of the single crystal at every one hour. The images are afterwards post-processed by applying Carl Zeiss' Axio Vision software (Gou et al., 2012).

In the experimental setup, small temperature differences and gradients cannot be measured, since this quantity is measured at a single point. Due this fact it is attractive to analyze, the temperature field within the entire growth cell numerically.

4. Simulations and analysis of the results

4.1. Validation of the finite-difference (FD) solver

In the present study, the FD method is adopted to solve for energy and species due to the large ratio between the value of thermal diffusivity and of mass diffusion coefficient; the corresponding Lewis number (the ratio between thermal diffusivity and mass diffusion) is of the order of $10^2 - 10^3$. Finite differences are more suitable for low values of the diffusion coefficient, since LBM becomes numerically unstable at very low non-dimensional diffusion coefficients, the relaxation time τ becoming close to 0.5.

4.1.1. Self-convergence of FD method

As known, LBM is of second-order accuracy for the phase-field model (Tan et al., 2023). Here, the accuracy of the finite-difference method is checked by considering only diffusion for a case with non-homogeneous concentrations. In this test-case, periodic boundaries are implemented in a 2D box of size $[-1, 1] \times [-1, 1]$ mm.

The concentration profile is set as a Gaussian hill following (Krüger et al., 2017; Fedi et al., 2010):

$$C(\mathbf{x}, t) = \frac{\Psi_0}{2\pi \sqrt{|\sigma_t|}} \exp\left(-\frac{1}{2} \sigma_t^{-1} : \mathbf{x}^2 \right). \tag{24}$$
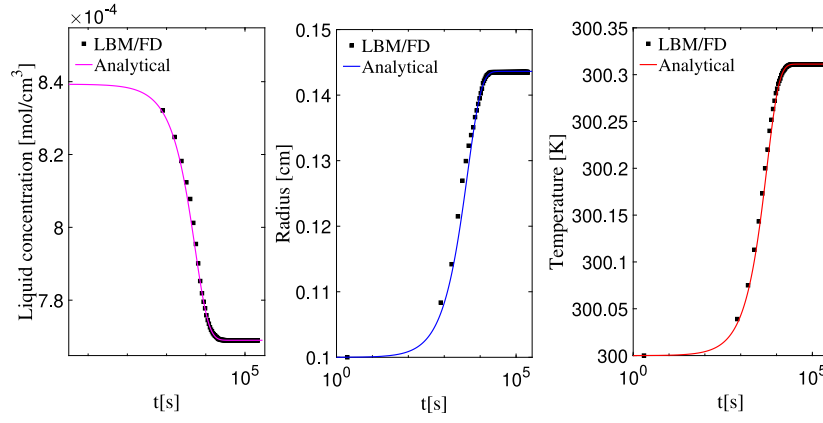
Fig. 4. Plots showing average concentration (left), crystal radius (center) and average temperature (right) as function of time as obtained from the hybrid LBM/FD solver, compared with analytical solution. Note the horizontal logarithmic scale due to the long duration of the process.
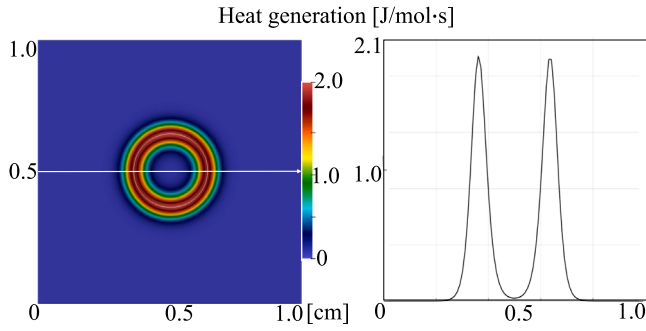

Fig. 5. Molar heat generation during growth of spherical crystal at time $t = 1$ hour.
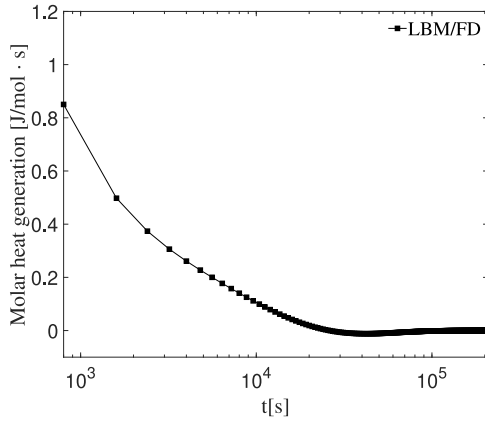

Fig. 6. Evolution of average molar heat generation with time connected to spherical crystal growth.
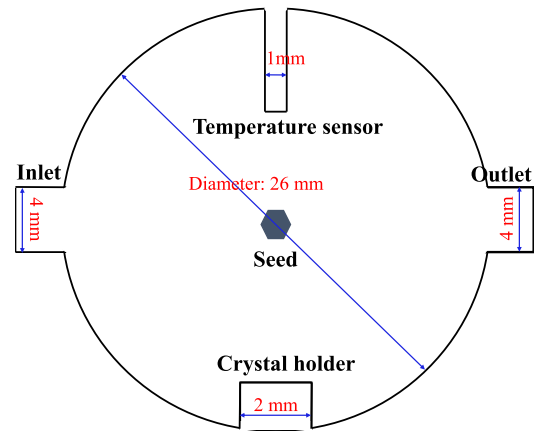

Fig. 7. Reactor geometry employed for all 2D simulations.
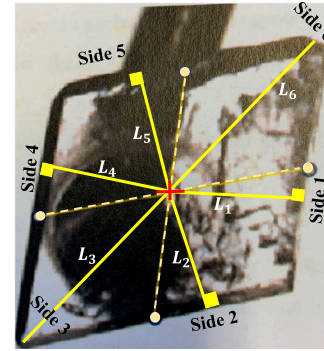
Fig. 8. Method used to number the crystal sides and the associated normal directions (Bianco, 2009).

where $\Psi_0 = 2\pi\sigma_0^2$ with initial variance $\sigma_0 = 0.01$ mm. The tensor $\boldsymbol{\sigma}_t = \sigma_0^2\mathbf{I} + 2t\mathbf{D}$, $|\boldsymbol{\sigma}_t|$ are the determinant value and $\boldsymbol{\sigma}_t^{-1}$ is inverse matrix of $\boldsymbol{\sigma}_t$, respectively. Quantity $\mathbf{I}$ is the unit matrix. Note that σ_0 is small enough in the present case, so that periodic boundary conditions are suitable.

The diffusion tensor in 2D:

$$\mathbf{D} = \begin{bmatrix} D_{xx} & D_{xy} \\ D_{yx} & D_{yy} \end{bmatrix} \tag{25}$$

Therefore, $\boldsymbol{\sigma}_t$ is:

$$\boldsymbol{\sigma}_t = \begin{bmatrix} \sigma_0^2 + 2tD_{yy} & 2tD_{yx} \\ 2tD_{xy} & \sigma_0^2 + 2tD_{xx} \end{bmatrix} \tag{26}$$

here diffusion coefficient is set by: $D_{xy} = D_{yx} = 0$, $D_{xx} = D_{yy}$. The simulations are conducted using four different spatial resolutions, $\delta x \in \{0.04, 0.025, 0.02, 0.016\}$ mm. Since the overall size of the numerical domain is kept fixed, an improved spatial resolution automatically comes with a larger number of grid points. Then, the results are compared with the analytical solution (see Eq. (24)) at time $t = 10$s.

The l^2 relative error norm is calculated based on the concentration profiles over the entire domain. The l^2 norm is defined as:

$$E_{l^2} = \sqrt{\frac{\sum_i \left(C_i - C_{an,i}\right)^2}{\sum_i C_{an,i}^2}} \tag{27}$$

Table 2
Relative l^2 errors of the scalar variable C for different resolutions.

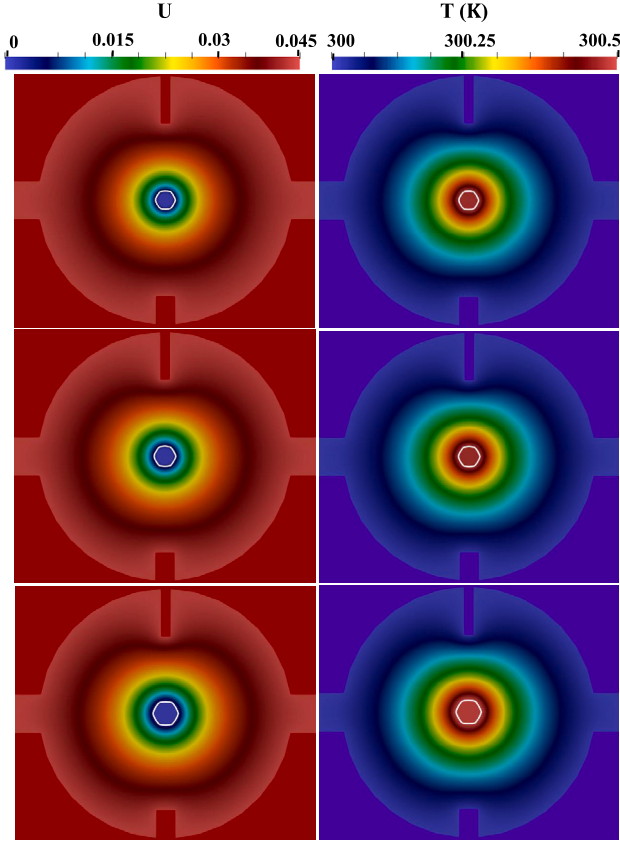| Numerical grid	50×50	80×80	100×100	125×125
E_{l^2}	5.0565	0.1787	0.0193	0.0081

Fig. 9. Instantaneous supersaturation and temperature fields in the growth cell for initial supersaturation $U_0 = 0.045$ at times $t = 4$ hours (top), 8 h (center), 16 h (bottom), respectively.

where C_i represents the concentration obtained numerically at a certain position in the box and C_{an} denotes the analytical solution from Eq. (24). The errors obtained from the different simulations are illustrated in Fig. 2.

As observed from this plot, the numerical scheme is convergent as the error decreases with resolution. Furthermore, as expected from theoretical analyses, a fourth-order convergence is obtained for the finite-difference solver.

Figs. 11 and 12 show the heat release process during phase-change from the liquid into the solid state at the interface of the crystal.

4.1.2. Limiting case: adiabatic single-crystal growth cell

In this section, in order to get rough insight regarding the temperature range possible, an adiabatic single-crystal growth cell is computed using mass and energy conservation for the purpose of verifying the proper function of the hybrid LBM/FD solver for describing single S-ma crystal growth rate and temperature within the cell.

The model is based on a square box in 3D (see Fig. 3) with a side length of 1 cm. The seed is set in the center of the box with initial radius $R = 0.1$ cm. The initial concentration of the supersaturated aqueous S-ma aqueous solution is 0.887 mmol/cm³ in this closed adiabatic system. The S-ma crystal keeps growing until the solution concentration reaches equilibrium. The liquid phase mass balance involving liquid phase concentration c reads:

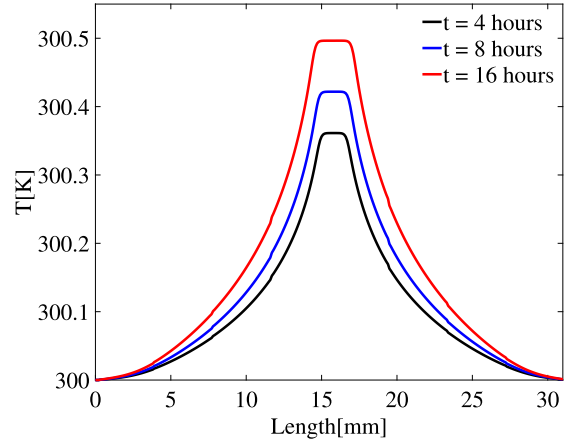$$V_L \frac{dc}{dt} = -k(T)A_{solid}(c - c_{sat}(T)) = -k(T)4\pi R^2(c - c_{sat}(T)) \quad (28)$$

Fig. 10. Temperature profile around the center-line of the numerical domain at times $t = 4$, 8 and 16 h, respectively.

where V_L is the volume of the adiabatic box (here, 1 cm³); variable $A_{solid} = 4\pi R^2$ is the surface area of the solid; $V_{solid} = \frac{4}{3}\pi R^3$ is its volume; $c_{sat}(T)$ is the saturation concentration (see Eq. (33)) and $k(T)$ the growth rate constant (see Eq. (34)), both at temperature T. The ordinary differential equation describing the liquid phase concentration c is:

$$\frac{dc}{dt} = -\frac{k(T)}{V_L}4\pi R^2(c - c_{sat}(T)) \quad (29)$$

The solid phase mass balance reads (assuming that the density does not depend on temperature, since temperature differences are expected to be low):

$$\rho_S \frac{dV_S}{dt} = \rho_S 4\pi R^2 \frac{dR}{dt} = k(T)4\pi R^2 M_S(c - c_{sat}(T)) \quad (30)$$

where ρ_S is the density of the mandelic acid crystal, M_S is the molar mass of the solid. The second ordinary differential equation describing radius is:

$$\frac{dR}{dt} = \frac{k(T)}{\rho_S}M_S(c - c_{sat}(T)) \quad (31)$$

The third ordinary differential equation representing energy (here in the form of temperature) is:

$$\frac{dT}{dt} = -\frac{\Delta H_{cryst}}{V_L \rho_L c_{p,L} + \frac{4}{3}\pi R^3 \rho_S c_{p,S}} k(T)4\pi R^2(c - c_{sat}(T)) \quad (32)$$

The value of specific heat capacity $c_{p,L}$ is that of water, and $c_{p,S}$ is from the S-mandelic acid, taken from Sapoundjiev et al. (2005). The saturation function for a mandelic acid aqueous solution is (Lorenz et al., 2002):

$$c_{sat}(T) = -0.005006 + 0.00001923T \quad (33)$$

where temperature T with unit K and the kinetic growth rate constant is:

$$k(T) = k_0 e^{-E/(RT)} \quad (34)$$

where k_0 is the crystal growth rate constant with the unit [cm/s]; E is the activation energy, with unit [J/mol]. Due to the small temperature range covered, the growth rate coefficient $k(T)$ was assumed to be constant in the temperature range between 20 and 30 °C. The value used is given in Table 1.

In the numerical simulation based on the hybrid LBM/FD solver, the spatial discretization is 0.01 cm (leading to a grid [$100 \times 100 \times 100$]) and the time-step is 0.005s. The physical parameters of S-ma are selected based on Table 1. Fig. 4 shows average concentration, crystal radius, and average temperature as function of time. It can be observed that the numerical solution obtained with the hybrid LBM/FD solver
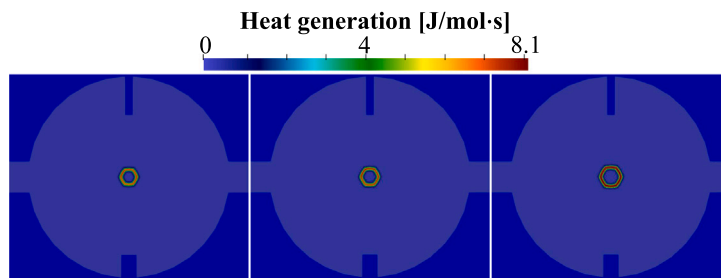
Fig. 11. Instantaneous heat generation at the interface of the crystal at times $t = 4$, 8 and 16 h (from left to right), respectively.
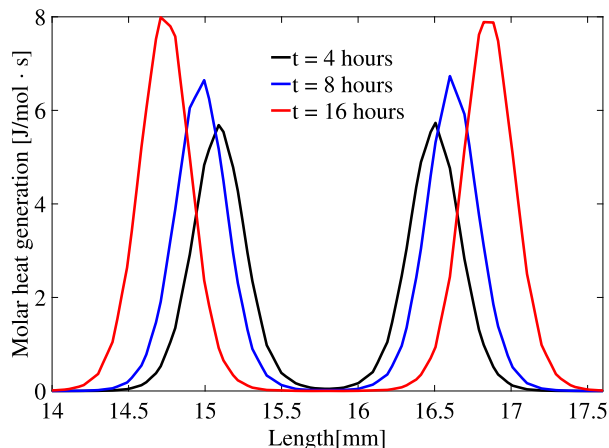

Fig. 12. Instantaneous heat generation along the centerline of the numerical domain at times $t = 4$, 8 and 16 h, respectively.

matches well with the analytical solutions derived from mass and energy conservation. Figs. 5 and 6 illustrate the heat release process during phase-change from the liquid into the solid state at the interface of the crystal. Eventually, the heat release is stopped when the crystal stops growing (equilibrium state has been reached). This successfully terminates the verification procedure for the developed numerical model. It can now safely be used to investigate growth rates and possible temperature effects for a single S-ma crystal.

4.2. Validation for S-ma crystal growth including temperature effects

4.2.1. Experiments vs. numerical simulation for different temperatures

An excellent agreement between numerical predictions and experimental observations was observed in a previous study when neglecting the influence of changes in temperature (Tan et al., 2023). In order to check now the ability of the solver to correctly describe S-ma crystal growth at different temperatures (from 20 °C to 30 °C), 2D simulations are carried out using the real reactor geometry. The reduction to two dimensions is justified by the fact that, in all conditions considered here, the crystal follows a platelet growth mode leading to a clear separation of scales between growth in axial or in planar directions, ensuring also symmetry of the flow field (Henniges et al., 2017). The 2D geometry used for the simulations is shown in Fig. 7. First, configurations are considered where forced convection is negligible. For all experiments presented in this section the initial seed is a hexagonal crystal. The initial supersaturation is $U = 0.045$, and the temperature is $T = 20$ °C, $T = 25$ °C, or $T = 30$ °C, respectively. The employed physical parameters have been given in Table 1. All simulations are carried out with a spatial resolution of $\delta x = 0.1$ mm. The interface thickness is set to $W_0 = 0.25$ mm, the relaxation time to $\tau_0 = 0.02$s, and the coupling coefficient $\lambda = 3$ was chosen as a standard value for the phase-field method for dendrite growth (Ramirez et al., 2004). At the walls of the reactor, zero-flux boundary conditions are applied to

Table 3
Comparison between experiments and simulations for initial supersaturation $U = 0.045$ as a function of temperature (Klukas, 2006).

Average growth rate [mm/h]	$T = 20$ °C	$T = 25$ °C	$T = 30$ °C
Experiments	0.011	0.023	0.0321
Simulations	0.0096	0.0222	0.0317

both the species and phase fields. A constant wall temperature (set as the value of T_1, see Fig. 1) is used as boundary condition for the energy equation. At the inlet a constant supersaturation is imposed, following the implementation described in Krüger et al. (2017) for the boundary condition.

In Table 3, G_{th} is the average growth rate (in mm/h) obtained as $G_{th} = (L_1 + L_2 + L_3 + L_4 + L_5 + L_6)/6t$ in both experiment and simulation. The comparison between computed and measured values points to a good agreement at all temperatures. L is the normal length from the center to every side of the crystal(see Fig. 8). It is observed that the S-ma growth rate increases with temperature. As far as can be judged from only 3 values (no other conditions have been investigated experimentally), a quite linear behavior is observed between temperature and growth rate in the range studied. It is now interesting to check the occurrence and strength of possible temperature gradients within this growth cell.

4.2.2. Occurrence of temperature gradients during crystal growth

Although the temperature of the single-crystal growth cell in the experimental setting is kept constant through the walls at the temperature of vessel V1, the growth of the crystal generates heat at the interface between liquid and solid phase. The Pt-100 sensor used for the temperature measurements in the experiment delivers only a point value and cannot be used to track possible gradients. Hence, in this section, the temperature field in the whole growth cell is studied numerically. The initial supersaturation is kept at $U_0 = 0.045$ as in the previous section.

In Fig. 9, it is seen that the highest temperature in the crystal as well as the solution temperature far from the crystal are still found at around 300 K. However, a maximum difference in temperature of the order of 0.5 °C is indeed observed within the cell, with a maximum temperature close to the interface. Though small, this shows that temperature differences do exist within the single-crystal growth cell. Since these differences appear locally, non-negligible temperature gradients will occur as well. Fig. 10 demonstrates that the temperature increase has a peak value in the range of the single crystal and decreases in the fluid phase to the wall of the cell.

4.2.3. Ventilation and temperature effects during S-ma crystal growth

In the real single-crystal reactor the incoming flow of (S)-mandelic acid in solution might have an impact on crystal growth rate and shape, as demonstrated in Tan et al. (2023) when neglecting temperature changes. The aim of the present section is to check this point for different Reynolds numbers, and to suggest the inclusion of baffles to support symmetrical growth.
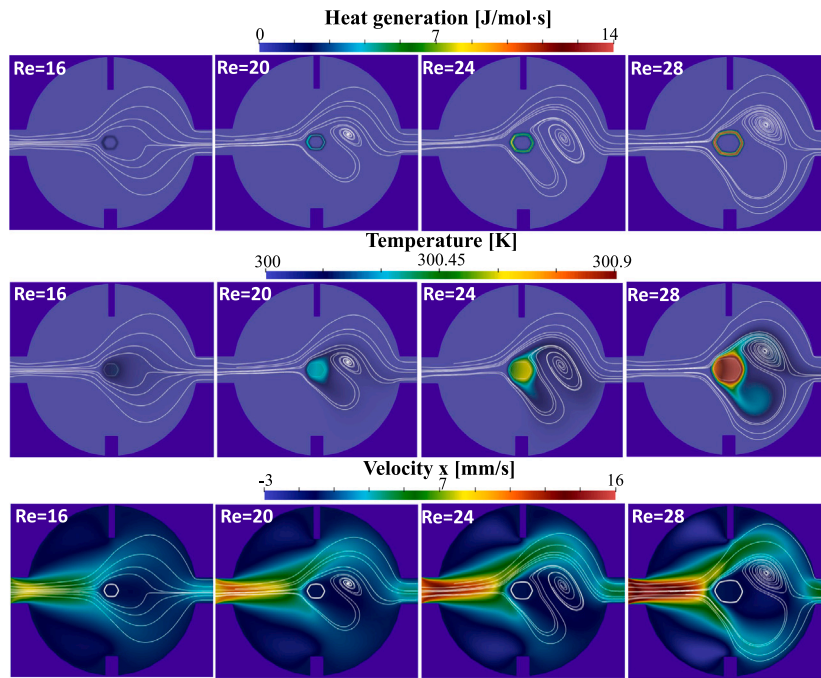
Fig. 13. Instantaneous fields of heat generation (top), temperature (center), velocity field (bottom) within the growth cell at time t = 16 hours for different Reynolds numbers Re = 16, 20, 24, and 28 (from left to right), respectively.
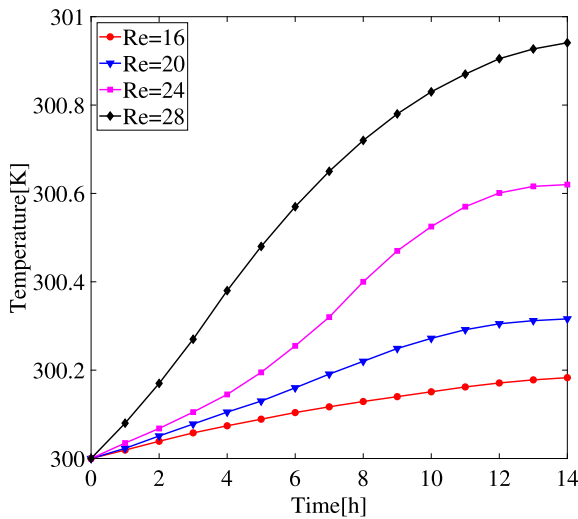

Fig. 14. Evolution of peak temperature with time within the cell for different Reynolds numbers Re = 16, 20, 24, and 28, respectively.

Fig. 15. 2D growth-cell geometry including baffles at different positions.

Effect of Reynolds number. The Reynolds number is defined as Re= $u_{in}L_D/\nu_f$, where L_D is the initial diameter of the circumscribed circle of the hexagonal crystal seed, ν_f is the kinematic viscosity of water, taken at 1 mm^2/s. The inlet velocity is set as u_{in} = 8, 10, 12 or 14 mm/s, respectively.

Fig. 13 shows that at higher Reynolds number, the crystal grows much faster. As a consequence, more heat is generated at the interface because of the intensive solute convection around the crystal. This effect dominates over the accelerated transport of heat away from the crystal by the flow. Overall, an increase of the maximum temperature with Re is observed around the single crystal (see Fig. 14).

Baffle. As seen from Fig. 13 (white lines in the bottom figure, showing the crystal boundary), the overall shape of the crystal varies considerably as function of the Reynolds number, and rapidly becomes
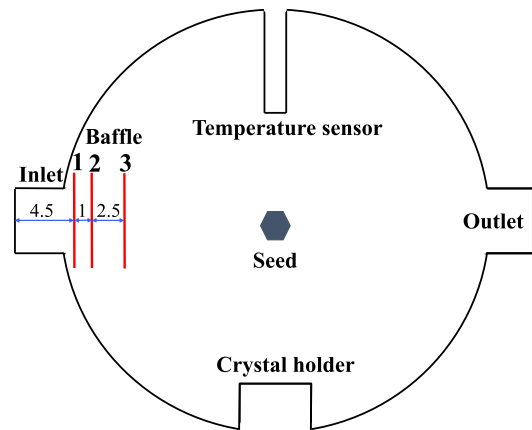
non-symmetric. However, the regularity of the crystal shape is a property of high interest regarding the performance of the final products. Therefore, it would be desirable to find a simple geometrical modification to the single-crystal growth cell, leading to isotropic growth rates and/or a desired final aspect ratio. For this purpose, a simple flat baffle has been included in the simulation domain in front of the inlet, in order to prevent a direct impact of the incoming flow onto the growing seed. Three different configurations (different positions) of the baffle have been compared. The resulting configurations are illustrated in Fig. 15; what is called configuration 0 is the original case, without any baffle.

Fig. 16 shows that ventilation effects are still visible with the baffle at position 1, much more than at other positions; this case leads to the faster crystal growth in vertical direction. The single crystal growth becomes more symmetric as the baffle is placed at a farther distance from the inlet of the growth cell. To quantify the effect of the baffles on the symmetry of the crystal, a quality parameter has been defined as $Q = \max(L_i)/\min(L_i)$ where index $i \in \{0, \ldots, 5\}$ covers the length
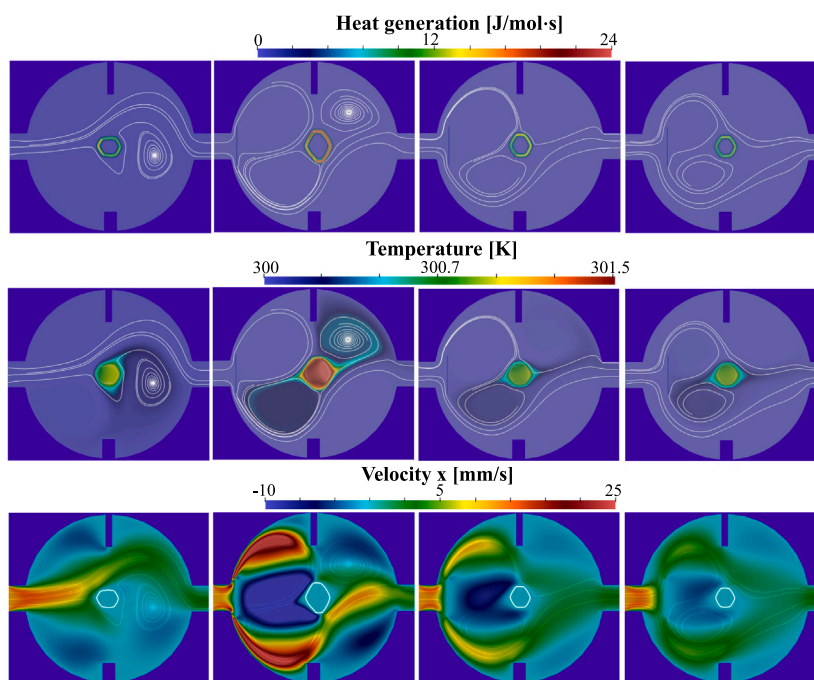
Fig. 16. Instantaneous fields of heat generation (top), temperature (center), velocity (bottom) at time $t = 16$ hours in the growth cell with the baffle placed at different positions (from left to right): (1) without baffle; (2) with baffle at position 1; (3) with baffle at position 2; (4) with baffle at position 3.
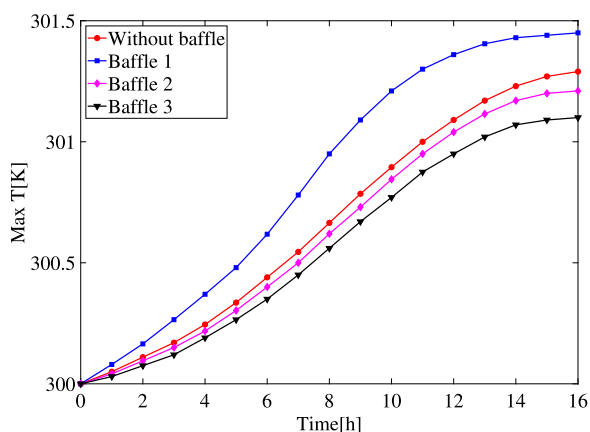

Fig. 17. Evolution of peak temperature with time for the baffles placed at different positions, for an initial temperature $T_0 = 300$ K.

Table 4
Impact of the different baffles (see Fig. 15) on the isotropy ratio.

Position	No baffle	Baffle 1	Baffle 2	Baffle 3
Q	1.29	1.73	1.16	1.12

5. Conclusions and perspectives

In this work, a hybrid LBM/finite-difference method has been used to model the growth of a single crystal of (S)-mandelic acid. LBM is used for the phase-field equation, while the finite-difference method is applied for the species and energy equations due to the high ratio between thermal and species diffusivity. Selected test-cases show that numerical stability can be achieved with the hybrid solver thanks to the finite-difference method. Successful verification and validation steps are documented. The results provide detailed information regarding the magnitude and dynamics of the temperature fields developing in the measuring cell during the growth process. The heat generation during phase change at the interface of the crystal leads overall to only small changes in temperature over the whole cell. These local changes in temperature lead to noticeable temperature gradients around the crystal interface. For all cases considered, a maximum temperature increase of almost 1.5 °C has been observed at the moving crystal interface where the temperature sensor is unable to measure it. In this particular case the molar heat generation at the interface can be probably neglected to address most questions of interest. However, convection can amplify temperature differences. Using a baffle located at a suitable position, ventilation and temperature effects can be minimized.

Declaration of competing interest

The authors declare that they have no known competing financial interests or personal relationships that could have appeared to influence the work reported in this paper.

Data availability

The data that has been used is confidential.

of all sides of the resulting crystal. Thus, parameter Q quantifies non-isotropic growth, with $Q = 1$ (the minimum value) corresponding to a perfectly isotropic growth, while an increasing value of Q corresponds to increasing non-isotropy. The values of crystal quality as obtained from all simulations after 16 h of growth are listed in Table 4. Overall, the baffle in position 3 should be preferred to get maximum isotropy and minimum temperature effects.

Fig. 17 shows the peak temperature as function of time for the different baffles. Baffle 1 corresponds to the large ventilation effects visible in Fig. 16; then, the crystal side facing the high flow velocity in vertical direction leads to a much larger growth rate there, generating much heat at the crystal interface.

Stuttgart-Höchstleistungsrechenzentrum Stuttgart (HLRS); all calculations for this publication were conducted with computing resources provided under project number 44216.

References

Alvarez Rodrigo, A., Lorenz, H., Seidel-Morgenstern, A., 2004. Online monitoring of preferential crystallization of enantiomers. Chirality 16 (8), 499–508.

Beckermann, C., Diepers, H.J., Steinbach, I., Karma, A., Tong, X., 1999. Modeling melt convection in phase-field simulations of solidification. J. Comput. Phys. 154 (2), 468–496.

Bianco, J., 2009. Single-Crystal Growth Kinetics in a Chiral System Master Thesis. Otto von Guericke University Magdeburg.

Boettinger, W.J., Warren, J.A., Beckermann, C., Karma, A., 2002. Phase-field simulation of solidification. Annu. Rev. Mater. Res. 32 (1), 163–194.

Briesen, H., 2006. Simulation of crystal size and shape by means of a reduced two-dimensional population balance model. Chem. Eng. Sci. 61 (1), 104–112.

Brittain, H.G., 2002. Mandelic acid. In: Analytical Profiles of Drug Substances and Excipients, Vol. 29. Elsevier, pp. 179–211.

Cartalade, A., Younsi, A., Plapp, M., 2016. Lattice boltzmann simulations of 3d crystal growth: Numerical schemes for a phase-field model with anti-trapping current. Comput. Math. Appl. 71 (9), 1784–1798.

Chakraborty, S., Chatterjee, D., 2007. An enthalpy-based hybrid lattice-boltzmann method for modelling solid–liquid phase transition in the presence of convective transport. J. Fluid Mech. 592, 155–175.

Chen, L.Q., Yang, W., 1994. Computer simulation of the domain dynamics of a quenched system with a large number of nonconserved order parameters: The grain-growth kinetics. Phys. Rev. B 50 (21), 15752.

Chlebus, E., 2006. Mandelic acid–a new medical peel. Dermatologia 282.

Cockburn, B., Shu, C.-W., Johnson, C., Tadmor, E., Shu, C.-W., 1998. Essentially Non-Oscillatory and Weighted Essentially Non-Oscillatory Schemes for Hyperbolic Conservation Laws. Springer.

Codan, L., Eckstein, C.F., Mazzotti, M., 2013. Growth kinetics of s-mandelic acid in aqueous solutions in the presence of r-mandelic acid. Cryst. Growth Des. 13 (2), 652–663.

Coquerel, G., 2006. Preferential Crystallization. Novel Optical Resolution Technologies, pp. 1–51.

Emelýanenko, V.N., Turovtsev, V.V., Fedina, Y.A., 2018. Experimental and theoretical thermodynamic properties of R-(-)-and S-(+)-mandelic acids. Thermochim. Acta 665, 37–42.

Fedi, A., Massabò, M., Paladino, O., Cianci, R., 2010. A new analytical solution for the 2d advection–dispersion equation in semi-infinite and laterally bounded domain. Appl. Math. Sci. 4 (75), 3733–3747.

Gänsch, J., Huskova, N., Kerst, K., Temmel, E., Lorenz, H., Mangold, M., Janiga, G., Seidel-Morgenstern, A., 2021. Continuous enantioselective crystallization of chiral compounds in coupled fluidized beds. Chem. Eng. J. 129627.

Gou, L., Lorenz, H., Seidel-Morgenstern, A., 2012. Investigation of a chiral additive used in preferential crystallization. Cryst. Growth Des. 12 (11), 5197–5202.

Henniges, M., Hosseini, S., Thévenin, D., Seidel-Morgenstern, A., Lorenz, H., 2017. Towards predictive numerical models for single crystal growth: validation of the velocity field. In: Proc. 24th International Workshop on Industrial Crystallization BIWIC2017.

Hosseini, S.A., 2020. Development of a Lattice Boltzmann-Based Numerical Method for the Simulation of Reacting Flows (Ph.D. thesis). Université Paris-Saclay & Otto-von-Guericke University.

Hosseini, S.A., Abdelsamie, A., Darabiha, N., Thévenin, D., 2020. Low-mach hybrid lattice boltzmann-finite difference solver for combustion in complex flows. Phys. Fluids 32 (7), 077105.

Hosseini, S.A., Berg, P., Huang, F., Roloff, C., Janiga, G., Thévenin, D., 2021. Central moments multiple relaxation time lbm for hemodynamic simulations in intracranial aneurysms: An in-vitro validation study using piv and pc-mri. Comput. Biol. Med. 131, 104251.

Hosseini, S.A., Coreixas, C., Darabiha, N., Thévenin, D., 2019a. Extensive analysis of the lattice boltzmann method on shifted stencils. Phys. Rev. E 100 (6), 063301.

Hosseini, S.A., Darabiha, N., Thévenin, D., 2019b. Lattice boltzmann advection-diffusion model for conjugate heat transfer in heterogeneous media. Int. J. Heat Mass Transfer 132, 906–919.

Hosseini, S.A., Darabiha, N., Thévenin, D., 2022. Low mach number lattice boltzmann model for turbulent combustion: flow in confined geometries. In: Proceedings of the Combustion Institute.

Hosseini, S.A., Safari, H., Darabiha, N., Thévenin, D., Krafczyk, M., 2019c. Hybrid lattice boltzmann-finite difference model for low mach number combustion simulation. Combust. Flame 209, 394–404.

Jeong, J.H., Goldenfeld, N., Dantzig, J.A., 2001. Phase field model for three-dimensional dendritic growth with fluid flow. Phys. Rev. E 64 (4), 041602.

Karma, A., Rappel, W.J., 1996. Phase-field method for computationally efficient modeling of solidification with arbitrary interface kinetics. Phys. Rev. E 53 (4), R3017.

Karma, A., Rappel, W.J., 1998. Quantitative phase-field modeling of dendritic growth in two and three dimensions. Phys. Rev. E 57 (4), 4323.

Klukas, L., 2006. Einzelkornuntersuchungen Zum Kristallwachstum in Chiralen Systemen. Internal Report, Magdeburg-Stendal University of Applied Sciences, Magdeburg.

Krüger, T., Kusumaatmaja, H., Kuzmin, A., Shardt, O., Silva, G., Viggen, E.M., 2017. The Lattice Boltzmann Method, Vol. 10. Springer International Publishing, pp. 4–15, (978-3).

Lin, G., Bao, J., Xu, Z., 2014. A three-dimensional phase field model coupled with a lattice kinetics solver for modeling crystal growth in furnaces with accelerated crucible rotation and traveling magnetic field. Comput. Fluids 103, 204–214.

Liu, X.-D., Osher, S., Chan, T., 1994. Weighted essentially non-oscillatory schemes. J. Comput. Phys. 115 (1), 200–212.

Lorenz, H., Sapoundjiev, D., Seidel-Morgenstern, A., 2002. Enantiomeric mandelic acid system melting point phase diagram and solubility in water. J. Chem. Eng. Data 47 (5), 1280–1284.

Lorenz, H., Seidel-Morgenstern, A., 2014. Processes to separate enantiomers. Angew. Chem. Int. Ed. 53 (5), 1218–1250.

Medvedev, D., Fischaleck, T., Kassner, K., 2006. Influence of external flows on crystal growth: Numerical investigation. Phys. Rev. E 74 (3), 031606.

Mullin, J.W., 2001. Crystallization. Elsevier.

Nestler, B., Wheeler, A., 2002. Phase-field modeling of multi-phase solidification. Comput. Phys. Commun. 147 (1–2), 230–233.

Patterson, J., Morris, E., 1994. Measurement of absolute water density, 1 c to 40 c. Metrologia 31 (4), 277.

Perlberg, A., Lorenz, H., Seidel-Morgenstern, A., 2005. Crystal growth kinetics via isothermal seeded batch crystallization: Evaluation of measurement techniques and application to mandelic acid in water. Ind. Eng. Chem. Res. 44 (4), 1012–1020.

Ramirez, J.C., Beckermann, C., s. Karma, A., Diepers, H.J., 2004. Phase-field modeling of binary alloy solidification with coupled heat and solute diffusion. Phys. Rev. E 69 (5), 051607.

Rojas, R., Takaki, T., Ohno, M., 2015. A phase-field-lattice boltzmann method for modeling motion and growth of a dendrite for binary alloy solidification in the presence of melt convection. J. Comput. Phys. 298, 29–40.

Sakane, S., Takaki, T., Ohno, M., Shibuta, Y., Shimokawabe, T., Aoki, T., 2018. Three-dimensional morphologies of inclined equiaxed dendrites growing under forced convection by phase-field-lattice boltzmann method. J. Cryst. Growth 483, 147–155.

Sapoundjiev, D., Lorenz, H., Seidel-Morgenstern, A., 2005. Determination of solubility data by means of calorimetry. Thermochim. Acta 436 (1–2), 1–9.

Schiedung, R., Tegeler, M., Medvedev, D., Varnik, F., 2020. Simulation of capillary-driven kinetics with multi-phase-field and lattice boltzmann method. Modelling Simul. Mater. Sci. Eng. 28 (6), 065008.

Shan, X., 2006. Analysis and reduction of the spurious current in a class of multiphase lattice boltzmann models. Phys. Rev. E 73 (4), 047701.

Shan, X., Yuan, X.F., Chen, H., 2006. Kinetic theory representation of hydrodynamics: a way beyond the Navier–Stokes equation. J. Fluid Mech. 550, 413–441.

Shu, C.-W., 2020. Essentially non-oscillatory and weighted essentially non-oscillatory schemes. Acta Numer. 29, 701–762.

Slack, G.A., 1979. The thermal conductivity of nonmetallic crystals. Solid state Phys. 34, 1–71.

Speedy, R.J., 1982. Stability-limit conjecture. an interpretation of the properties of water. J. Phys. Chem. 86 (6), 982–991.

Srisanga, S., Flood, A.E., Galbraith, S.C., Rugmai, S., Soontaranon, S., Ulrich, J., 2015. Crystal growth rate dispersion versus size-dependent crystal growth: Appropriate modeling for crystallization processes. Cryst. Growth Des. 15 (5), 2330–2336.

Subhedar, A., Galenko, P.K., Varnik, F., 2020. Diffuse interface models of solidification with convection: The choice of a finite interface thickness. Eur. Phys. J. Spec. Top. 229, 447–452.

Takaki, T., Ohno, M., Shibuta, Y., Sakane, S., Shimokawabe, T., Aoki, T., 2016. Two-dimensional phase-field study of competitive grain growth during directional solidification of polycrystalline binary alloy. J. Cryst. Growth 442, 14–24.

Tan, Q., Hosseini, S., Seidel-Morgenstern, A., Thévenin, D., Lorenz, H., 2022. Modeling ice crystal growth using the lattice boltzmann method. Phys. Fluids 34 (1), 013311.

Tan, Q., Hosseini, S., Seidel-Morgenstern, A., Thevenin, D., Lorenz, H., 2023. Mandelic acid single-crystal growth: Experiments vs numerical simulations. Commun. Comput. Phys. 33 (1), 77–100.

Tanner, J., 1983. Intracellular diffusion of water. Arch. Biochem. Biophys. 224 (2), 416–428.

Tourret, D., Song, Y., Clarke, A.J., Karma, A., 2017. Grain growth competition during thin-sample directional solidification of dendritic microstructures: A phase-field study. Acta Mater. 122, 220–235.

Vakili, S., Steinbach, I., Varnik, F., 2020. Multi-phase-field simulation of microstructure evolution in metallic foams. Sci. Rep. 10 (1), 1–12.

Walsh, S.D., Saar, M.O., 2010. Macroscale lattice-boltzmann methods for low peclet number solute and heat transport in heterogeneous porous media. Water Resour. Res. 46 (7).

Wang, H., Yuan, X., Liang, H., Chai, Z., Shi, B., 2019. A brief review of the phase-field-based lattice boltzmann method for multiphase flows. Capillarity 2 (3), 33–52.

Younsi, A., Cartalade, A., 2016. On anisotropy function in crystal growth simulations using lattice boltzmann equation. J. Comput. Phys. 325, 1–21.

Zhang, Y., Mao, S., Ray, A.K., Rohani, S., 2010. Nucleation and growth kinetics of (r)-mandelic acid from aqueous solution in the presence of the opposite enantiomer. Cryst. Growth Des. 10 (7), 2879–2887.

Zirdehi, E.M., Varnik, F., 2019. Non-monotonic effect of additive particle size on the glass transition in polymers. J. Chem. Phys. 150 (2), 024903.